1D-FDTD using MATLAB

Hung Loui, *Student Member, IEEE*

***Abstract*— This report presents a simple 1D implementation of the Yee FDTD algorithm using the MATLAB programming language. The fields E_x and H_y are simulated along the line $X = Y = 0$, i.e. propagation along the $\hat{z}$ axis. Source implementation and the effects of various boundaries such as PEC, PMC, Mur on the incident/scattered/total fields are subsequently investigated. The goal of this project is to exercise the basic parts of a FDTD code in the simplest system.**

***Index Terms*— 1D FDTD, Gaussian Pulse.**

I. Introduction

THE finite difference time domain (FDTD) method has been used extensively in the modelling of electromagnetic wave scattering from complex none-canonical objects. A comprehensive coverage, including a historical recount of the FDTD development can be found in [1]. There are also various books available which contain basic codes; [2] gives many good examples in C. We choose MATLAB as our coding language because of its comprehensive library of graphics routines. It is relatively straight forward to produce animations using MATLAB; this is often critical to the understanding of a working FDTD algorithm.

Due to the large amount of book-keeping required in any full 3D-FDTD code, it is common to reduce the dimensionality down to 1D for pedagogical purposes. Most of the equations in this report can be found in other texts, however, we have listed them here for the reason of continuity. A working FDTD code must propagate waves properly, handle various boundaries, and calculate useful modelling results. This paper addresses all of the above in a step by step process and has the following outline:

- Section II describes the reduction of Maxwell's equations from 3D to 1D and its subsequent FDTD implementation using Yee's algorithm. Formulations of the source, PEC, PMC, Mur and Scattered/Total Field (SF/TF) boundaries are also shown.
- Section III describes and verifies results of PEC, PMC, Mur and SF/TF boundary simulations.
- Section IV uses SF/TF and Mur boundaries to analyze Guassian pulse reflections from dielectric slabs of various thicknesses.
- Section V provides a conclusion to the overall experiment.

Report initiated on September 11, 2004. This work was supported by the University of Colorado, Course #: ECEN-6006, Special topics - Numerical Methods in Photonics.

Hung Loui is with the Department of Electrical and Computer Engineering, University of Colorado, Campus Box 425, Boulder, CO 80309-0425, USA. (e-mail: louih@ucsu.colorado.edu)

II. Formulation

A. Reduction of Maxwell's equations to 1D

The 3D source free $(\vec{J} = 0)$ Maxwell's curl equations of a homogeneous medium are:

$$\nabla \times \vec{E} = -\mu \frac{d\vec{H}}{dt} \longrightarrow \begin{cases} \frac{\partial E_z}{\partial y} - \frac{\partial E_y}{\partial z} = -\mu \frac{\partial H_x}{\partial t} \\ \frac{\partial E_x}{\partial z} - \frac{\partial E_z}{\partial x} = -\mu \frac{\partial H_y}{\partial t} \\ \frac{\partial E_y}{\partial x} - \frac{\partial E_x}{\partial y} = -\mu \frac{\partial H_z}{\partial t} \end{cases} \tag{1}$$

$$\nabla \times \vec{H} = \epsilon \frac{d\vec{E}}{dt} \longrightarrow \begin{cases} \frac{\partial H_z}{\partial y} - \frac{\partial H_y}{\partial z} = \epsilon \frac{\partial E_x}{\partial t} \\ \frac{\partial H_x}{\partial z} - \frac{\partial H_z}{\partial x} = \epsilon \frac{\partial E_y}{\partial t} \\ \frac{\partial H_y}{\partial x} - \frac{\partial H_x}{\partial y} = \epsilon \frac{\partial E_z}{\partial t} \end{cases} \tag{2}$$

For a $\hat{z}$-directed, $\hat{x}$-polarized TEM wave $(H_z = E_z = 0)$, incident upon a modeled geometry with no variations in the $\hat{x}$ and $\hat{y}$ direction, i.e. $\frac{\partial}{\partial x} = \frac{\partial}{\partial y} = 0$; equations (1) and (2) reduce down to the 1D case:

$$\frac{\partial E_x}{\partial z} = -\mu \frac{\partial H_y}{\partial t} \tag{3}$$

$$\frac{\partial H_y}{\partial z} = -\epsilon \frac{\partial E_x}{\partial t} \tag{4}$$

Combining the partial space derivatives of (3) with the partial time derivative of (4) or vice versa produces the 1D scalar wave equation:

$$\left[\frac{\partial^2}{\partial z^2} - \epsilon\mu \frac{\partial^2}{\partial t^2}\right] \psi = 0, \tag{5}$$

where ψ represents either E_x or H_y. In the case of free-space where $\epsilon = \epsilon_0$ and $\mu = \mu_0$, equation (5) takes on the familiar form:

$$\left[\frac{\partial^2}{\partial z^2} - \frac{1}{c^2} \frac{\partial^2}{\partial t^2}\right] \psi = 0 \tag{6}$$

where $c = \frac{1}{\sqrt{\epsilon_0 \mu_0}}$ is the speed of light in vacuum.

B. 1D time advancement equations

Although the 1D scalar wave equation (5) can be solved directly by centered 2nd differences [3], it is not robust for solutions of problems that depend on both $\vec{E}$ and $\vec{H}$. In 1966, Kane Yee proposed an algorithm [4] where the first order electric (3) and magnetic (4) equations are coupled via interlinked time and space grids. Because the underlying implementation of the Yee algorithm mimics the principle of a time varying electric field producing a time vary magnetic field and vice versa, solutions of more general class of problems can be handled robustly. Using Fig. 1 as a guide, the discrete

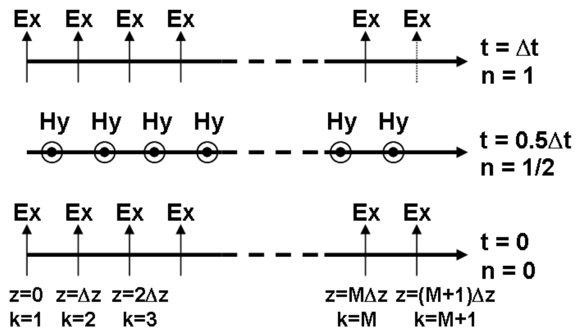

Fig. 1. 1D space-time chart of the Yee algorithm showing central differences for the space derivatives and leapfrog over the time derivatives. k represent electric field node numbers and n is the time step.

update equations in time are:

$$\frac{H_y|_{k+1/2}^{n+1/2} - H_y|_{k+1/2}^{n-1/2}}{\Delta t} = -\frac{1}{\mu}\frac{E_x|_{k+1}^{n} - E_x|_{k}^{n}}{\Delta z} \tag{7}$$

$$\frac{E_x|_{k}^{n+1} - E_x|_{k}^{n}}{\Delta t} = -\frac{1}{\epsilon}\frac{H_y|_{k+1/2}^{n+1/2} - H_y|_{k-1/2}^{n+1/2}}{\Delta z} \tag{8}$$

Since a majority of the programming languages can not handle none integer array indexes, equations (7) and (8) must be converted to a pseudo form where only integer array indexes are used:

```
Hy(1 to M)=0;
Ex(1 to M+1)=0;
For n=1 to total # of time steps,
 Ex(1)=source(n);
 For k=1 to M,
  Hy(k)=Hy(k)-dt/mu(k)*(Ex(k+1)-Ex(k))/dz;
 end
 For k=2 to M,
  Ex(k)=Ex(k)-dt/ep(k)*(Hy(k)-Hy(k-1))/dz;
 end
end
```

The first few lines of code initialize the E_x and H_y space vectors to zero; notice that the E_x vector has one additional element at the end. The first For loop is the time stepping loop, where the first Ex node is updated by the source and subsequent inner For loops update nodes of E_x and H_y up to M. The M+1 E_x nodes are not updated after initialization because the M+1 H_y nodes do not exist after the first full time step. Notice that the leap-frogging in time is implicitly build into the code, i.e. there are no time subscripts anywhere. The line where `Hy(k)=Hy(k)-dt/mu(k)*(Ex(k+1)-Ex(k))/dz` has the following meaning: the `Hy(k)`, `Ex(k+1)` and `Ex(k)` on the right is from the previous half time step, whereas the `Hy(k)` on the left is the current time step. Because MATLAB is a high level language, the above pseudo code is reduced to just a few lines:

```
Hy(1:M)=0;
Ex(1:M+1)=0;
For n=1:N,
  Ex(1)=source(n);
  Hy=Hy-dt./mu.*diff(Ex)/dz;
  Ex(2:M)=Ex(2:M)-dt./ep.*diff(Hy)/dz;
end
```

Using the above code as the 1D-FDTD core, implementations of sources and various other boundary conditions can be easily appended.

C. Source

Let the grid be filled with free space. We proceed to launch a modulated Gaussian pulse into the grid by directly driving E_x at the boundary $z = 0, k = 1$. Let us choose the modulation frequency so that its wavelength is $\lambda_0 = 0.5\mu m$ (green light) and select a Gaussian pulse width large enough to see about 5 cycles of this modulation. We also would like the grid to be long enough in $\hat{z}$ so that the modulated Gaussian pulse fills at most 1/5 of z. We define the modulation signal by:

$$f_0 = \frac{c}{\lambda_0} = \frac{1}{\tau_0} \tag{9}$$

$$m(t) = \sin(2\pi f_0\, t) \tag{10}$$

where τ_0 is the period of the modulation signal $m(t)$. A Gaussian pulse centered at t_c is defined by

$$g(t) = e^{-(t-t_c)^2/2\sigma^2} \tag{11}$$

Let $t_c = 5\tau_c/2$ so that the Gaussian pulse is centered at half of the total 5 cycles of the modulation signal. σ can be determined by requiring that t_c be confined within the full width at half maximum (FWHM) [5] of the Gaussian pulse or

$$\sigma = \frac{t_c}{FWHM} = \frac{t_c}{2\sqrt{2\ln 2}}. \tag{12}$$

Multiplication of (10) with (11) produces the continuous modulated Gaussian source:

$$E_x(t) = \sin(2\pi f_0\, t)e^{-(t-t_c)^2/2\sigma^2}; \tag{13}$$

where it's corresponding discrete version is:

$$E_x(n) = \sin(2\pi f_0\, n\Delta t)e^{-(n\Delta t-t_c)^2/2\sigma^2}. \tag{14}$$

To calculate the grid length so that the modulated Gaussian

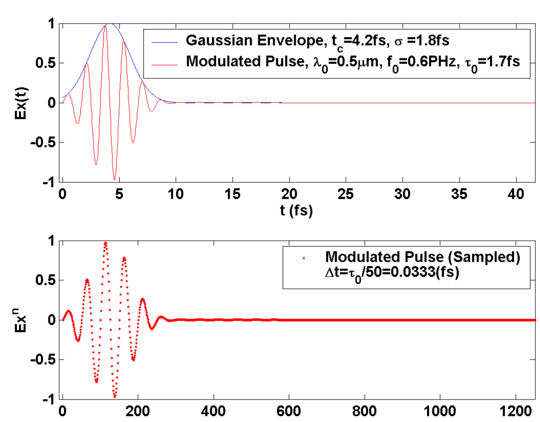

Fig. 2. Modulation of a Gaussian pulse using a 0.6PHz Sine wave.

pulse fills at most $1/5$ of z we simply multiply the pulse length of $5\lambda_0$ by 5.

D. PEC and PMC Boundary

Perfect electric conductor (PEC) and perfect magnetic conductor (PMC) boundaries are specified by simply setting the boundary electric field node $E_x = 0$ or the boundary magnetic field node $H_y = 0$, respectively.

E. 1st order Mur Boundary

Equations describing the 1st order Mur boundary is given in the notes [3]. We will update those equations so that they are consistent with the notation used here. To place a Mur radiation boundary at node M or the last electric field node on the right:

$$E_x|_M^{n+1} = E_x|_{M-1}^n + \frac{c\Delta t - \Delta z}{c\Delta t + \Delta z}(E_x|_{M-1}^{n+1} - E_x|_M^n). \quad (15)$$

To place a Mur radiation boundary at node 1 or the first electric field node on the left:

$$E_x|_1^{n+1} = E_x|_2^n + \frac{c\Delta t - \Delta z}{c\Delta t + \Delta z}(E_x|_2^{n+1} - E_x|_1^n). \quad (16)$$

F. Scattered/Total Field Boundary

Formulation of the 1D Scattered/Total field boundary can be found in [1]. However, because we are dealing with different set of field components than one does [1], the field correction factors differ in sign. It is therefore necessary for us to re-derive the correct update equations.

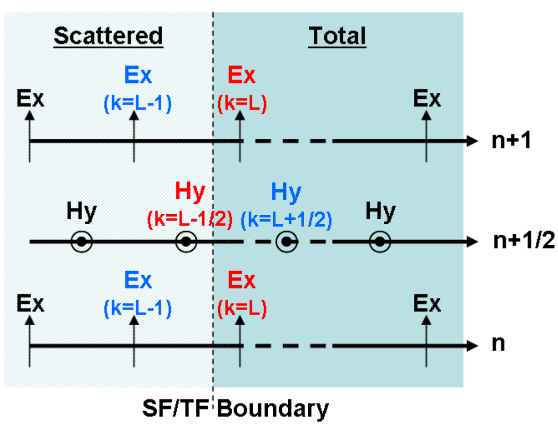

Fig. 3. Scattered/Total field boundary diagram. Color nodes are involved in the formulation of the boundary update equations; red nodes require correction.

Let the Scattered/Total field boundary be on the immediate left of the electric node L; if field types were the same on both sides of the boundary (both scattered or both total) then equations (7)-(8) can be used to update the corresponding field in time. However, because we had intended for the field on the left of the boundary to be the scattered field and on the right the total field, if equation (7) for the $H_y|_{L-1/2}$ node is updated on the $n+1/2$ time step, then in actuality it did the following:

$$H_y^{sca}|_{L-1/2}^{n+1/2} = H_y^{sca}|_{L-1/2}^{n-1/2} - \frac{\Delta t}{\mu}\frac{E_x^{tot}|_L^n - E_x^{sca}|_{L-1}^n}{\Delta z}. \quad (17)$$

Notice that the $E_x|_L^n$ node is a total field node. For consistency we must use the same field types when performing the $H_y|_{L-1/2}$ node update and since the $H_y|_{L-1/2}$ node lies on the scattered side of the boundary L, all field used in its update equation must be of the scattered type. Therefore, (17) should in fact be

$$H_y^{sca}|_{L-1/2}^{n+1/2} = H_y^{sca}|_{L-1/2}^{n-1/2} - \frac{\Delta t}{\mu}\frac{E_x^{sca}|_L^n - E_x^{sca}|_{L-1}^n}{\Delta z}. \quad (18)$$

We can make use of

$$-E_x^{sca}|_L^n = -E_x^{tot}|_L^n + E_x^{inc}|_L^n \quad (19)$$

to correct (17) so that it is equivalent to (18), and the resulting equation is

$$\underbrace{H_y^{sca}|_{L-1/2}^{n+1/2}}_{(18)} = \underbrace{H_y^{sca}|_{L-1/2}^{n+1/2}}_{(17)} + \frac{\Delta t}{\mu\Delta z}E_x^{inc}|_L^n. \quad (20)$$

A similar argument can be made for the $E_x|_L$ node, if equation (8) is updated on the $n+1$ time step, then in actuality it did the following:

$$E_x^{tot}|_L^{n+1} = E_x^{tot}|_L^n - \frac{\Delta t}{\epsilon}\frac{H_y^{tot}|_{L+1/2}^{n+1/2} - H_y^{sca}|_{L-1/2}^{n+1/2}}{\Delta z}. \quad (21)$$

Notice that the $H_y|_{L-1/2}^{n+1/2}$ node is a scattered field node. For consistency we must use the same field types when performing the $E_x|_L$ node update and since the $E_x|_L$ node lies on the total side of the boundary L, all field used in its update equation must be of the total type. Therefore, (21) should in fact be

$$E_x^{tot}|_L^{n+1} = E_x^{tot}|_L^n - \frac{\Delta t}{\epsilon}\frac{H_y^{tot}|_{L+1/2}^{n+1/2} - H_y^{tot}|_{L-1/2}^{n+1/2}}{\Delta z}. \quad (22)$$

We can make use of

$$-H_y^{tot}|_{L-1/2}^{n+1/2} = -H_y^{sca}|_{L-1/2}^{n+1/2} - H_y^{inc}|_{L-1/2}^{n+1/2} \quad (23)$$

to correct (21) so that it is equivalent to (22), and the resulting equation is

$$\underbrace{E_x^{tot}|_L^{n+1}}_{(22)} = \underbrace{E_x^{tot}|_L^{n+1}}_{(21)} + \frac{\Delta t}{\epsilon\Delta z}H_y^{inc}|_{L-1/2}^{n+1/2}. \quad (24)$$

The above formulations illustrate that only nodes immediately to the left and right of the boundary L need modification; this means that the original computer algorithm used to update equations (7)-(8) which are equivalent to (17) and (21) can execute as before, with modifications (18) and (22) performed afterwards. However, there is one catch, the correction equations (18) and (22) now require incident field components $E_x^{inc}|_L^n$ and $H_y^{inc}|_{L-1/2}^{n+1/2}$ be defined. There are two ways to accomplish this task, one way is to define $E_x^{inc}|_L^n$ and compute $H_y^{inc}|_{L-1/2}^{n+1/2}$ based on Maxwell's equations (which involves an impedance factor and a phase shift); the other way is to simply propagate the incident field in its own FDTD grid having the same Δz and Δt relationship as that for the scattered and total field. This latter approach ensures that all field types, i.e. incident, scattered and total suffer the same grid dispersion (see Section III), therefore it is implemented in the actual code.

III. Results

Having described formulations and basic pseudo code implementations of various parts of the one-dimensional FDTD algorithm, we now turn to results and verification.

A. Initialization

Initialization should be performed at the beginning of a simulation. Fig. 4 shows the initialized 1D space grid of $E_x(k)$ and $H_y(k)$ at time $t = 0$fs or $n = 0$, where n is the time index. The grid spacing is choosing to be $\Delta z = \lambda_0/20 = c\Delta t$; this is equivalent to sampling the input signal E_x in time at $\tau/20$, where $\tau = \lambda_0/c = 1/f_0$ is the period of the modulation signal. A probe is placed at the center of the grid for sampling E_x

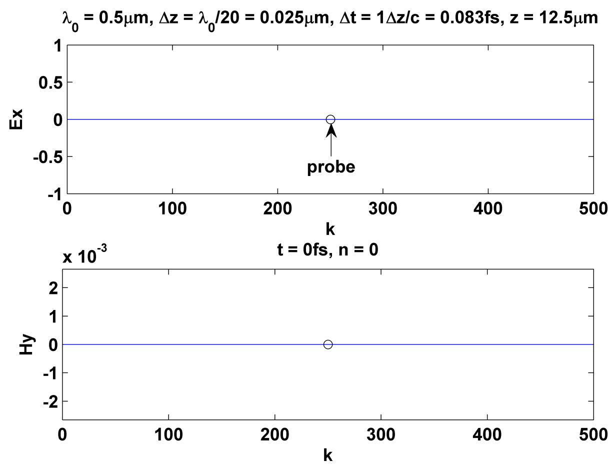

Fig. 4. Space grid initialization at time $t = 0$(fs). $E_x|_k$ and $H_y|_k$ nodes are set to initial values of 0(V/m) and 0(A/m), respectively. A sampling probe is placed at the center of the grid. No boundary conditions are explicitly specified anywhere.

and H_y pulses in time as they pass by. We will first operate at the magic time step $\Delta z = c\Delta t$ then shift off and adjust the spatial sampling to observe numerical dispersion.

B. PEC verification

In this section, we will enforce a PEC boundary condition at $z = z_{max} = 12.5\mu m$ and let the code run sufficiently long for the modulated Gaussian pulse to pass the probe point, bounce off the PEC at z_{max} or $k = M$ and pass the probe point again. For clarity, we will first follow the pulse closely in space, take snap shots of it at different times and then display the probe data later. Figures (5-7) show these snap shots of $E_x(k)$ and $H_y(k)$ at different times. The first thing to notice is the red PEC boundary at $z = z_{max}$ in all of the figures; it is also important to note that the amplitude of $H_y(k)$ is at all times a factor of $\eta_0 = \sqrt{\mu_0/\epsilon_0}$ smaller than that of $E_x(k)$. The pulse initiates from the left most electric field node in Fig. 5, propagates pass the probe point in Fig. 6 and finally collides with the PEC in Fig. 7.

From basic electromagnetic theory, we expect the tangential electric field to be zero on the PEC; therefore the reflected electric field must be 180 degrees out of phase compared to that of the incident field. This result is shown in Fig. 7 by comparing the incident $E_x(k)$ before colliding with the PEC (a) to the reflected $E_x(k)$ after colliding with the PEC (c); remember that the leading edge of the incident pulse is to

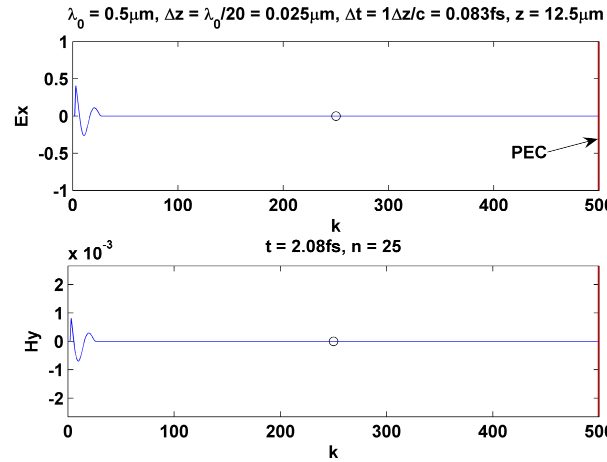

(a) Pulse entering from the left at t=2.08fs and n=25.

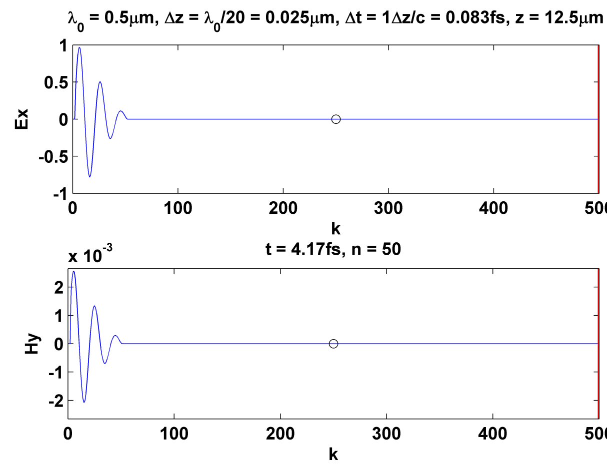

(b) Pulse propagating to the right at t=4.17fs and n=50.

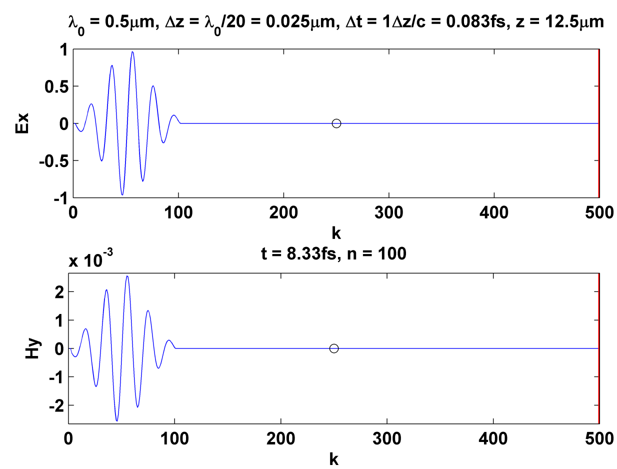

(c) Entire pulse entered space grid at t=8.33fs and n=100.

Fig. 5. $E_x(k)$ and $H_y(k)$ at (a) t=2.08fs (b) 4.17fs and (c) 8.33fs. Notice that by (c) the entire pulse fit approximately 1/5th of the total distance z of $12.5\mu m$; and there are exactly $k = 500$ electric nodes or $499\Delta z$ in z. The red vertical line at the boundary $z = z_{max} = 12.5\mu m, k = M = 500$ is the PEC.

the right whereas the leading edge of the reflected pulse is to the left. The 180 degree phase shift is more obvious if one compares $E_x(k)$ to $H_y(k)$ before and after colliding with the PEC in fig. 7(a) and (c), respectively.

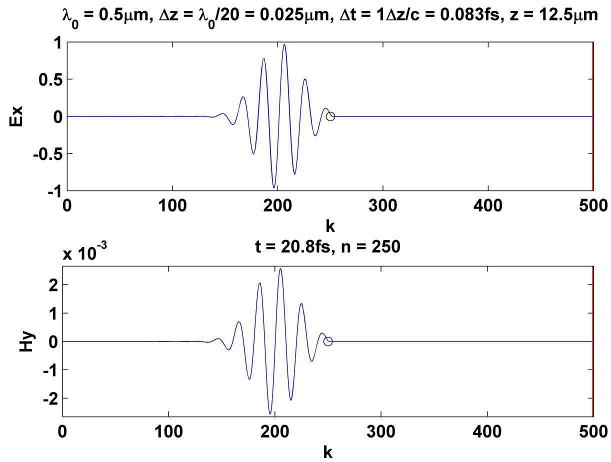

(a) Pulse approaching probe at t=20.8fs and n=250.

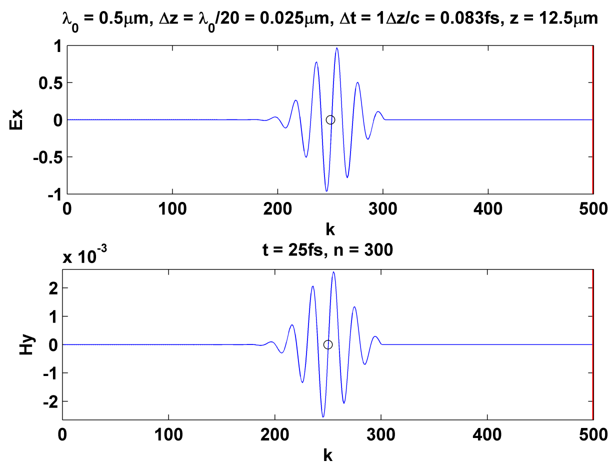

(b) Pulse passing the probe at t=25fs and n=300.

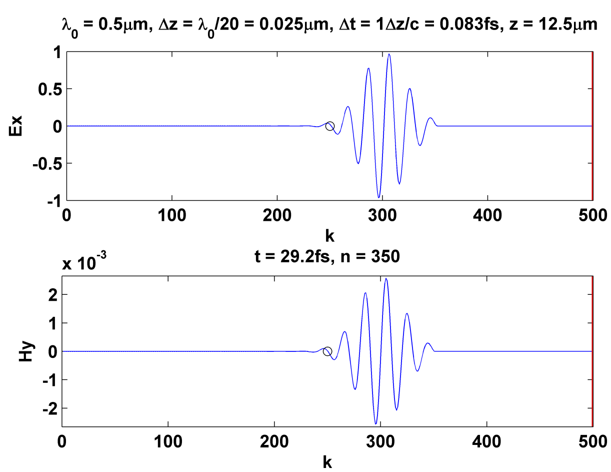

(c) Pulse approaching the PEC at t=29.2fs and n=350.

Fig. 6. $E_x(k)$ and $H_y(k)$ (a) right before the probe at t=20.8fs (b) passing the probe at t=25fs and (c) approaching the PEC at t=29.2fs. This demonstrates that the probe is merely a measuring device and does not alter the waveform in anyway.

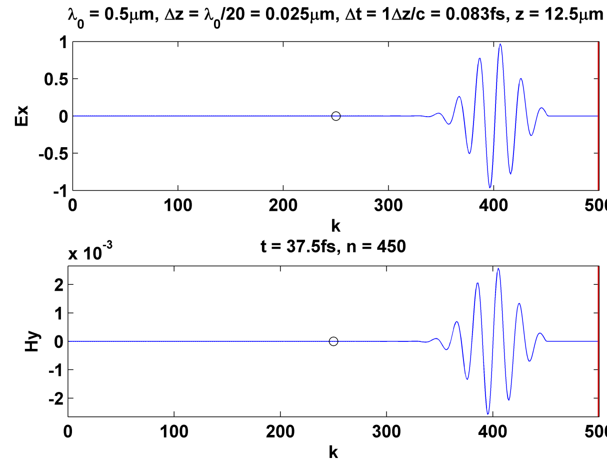

(a) Pulse approaching the PEC at t=37.5fs and n=450.

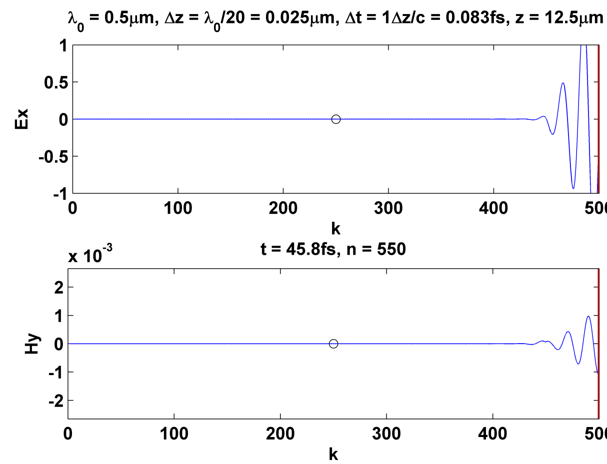

(b) Pulse colliding with the PEC at t=45.8fs and n=550.

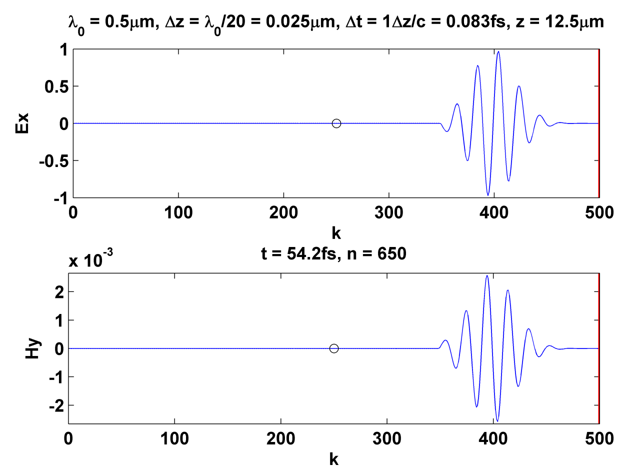

(c) Pulse reflected from the PEC at t=54.2fs and n=600.

Fig. 7. $E_x(k)$ and $H_y(k)$ (a) before the PEC at t=37.5fs (b) colliding with the PEC at t=45.8fs and (c) reflected from the PEC at t=54.2fs. Notice the constructive interference between the incident E_x and the reflected E_x at (b); because H_y and E_x differ in phase after reflection, while E_x is constructive interfering with maximum amplitude greater than unity, H_y is destructive interfering, this is why H_y shows decrease in overall amplitude compared to E_x in (b).

During the collision, part of the incident pulse reflects off the PEC and interferes with its own trailing tail; at the time of Fig. 7(b), this interference happens to be constructive in E_x but destructive in H_y due to the phase difference of π between them. The sampling probe at the center of the grid simply saves E_x and H_y at $k =$`probe_pos` for each time step n; i.e. probe data vectors are of length n and do not interact with the field vectors in any other way.

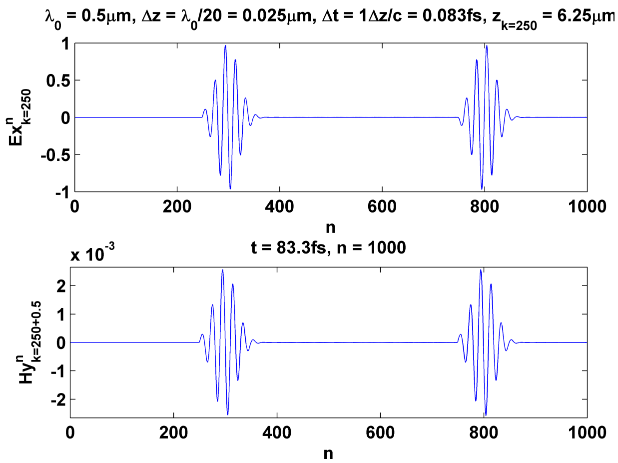

Fig. 8. Probe data of E_x and H_y at grid position $k = 250$ and $k = 250.5$ respectively, as a function of time step n. The total simulated duration was 83.3fs or $n = 1000$.

Fig. 8 displays E_x and H_y fields at the probe location of $k = 250$ and $k = 250.5$ respectively, for a total simulation duration of 83.3fs; it clearly shows that the PEC at $z = z_{max}$ or $n = 500$ caused E_x to invert while leaving H_y un-altered.

C. PMC

We now replace the PEC (red) at $z = z_{max}$ by a PMC (green) and repeat the steps from the previous section. For brevity, we will only show the pulse before and after the PMC as snaps shots in space, and let the probe keep a record of its journey in time.

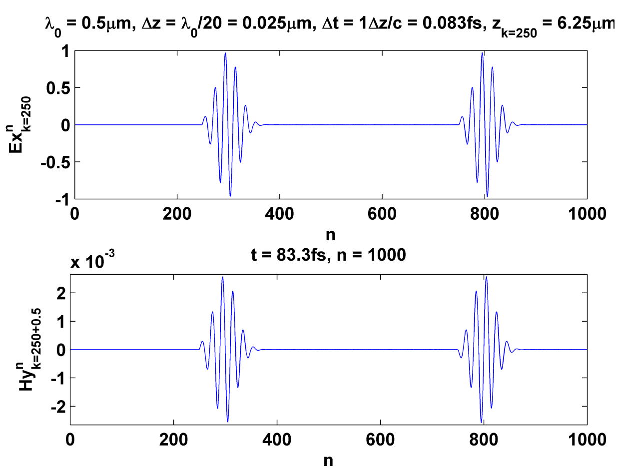

Fig. 9. PMC probe data of E_x and H_y at grid position $k = 250$ and $k = 250.5$ as a function of time step n. The total simulated duration was 83.3fs or $n = 1000$.

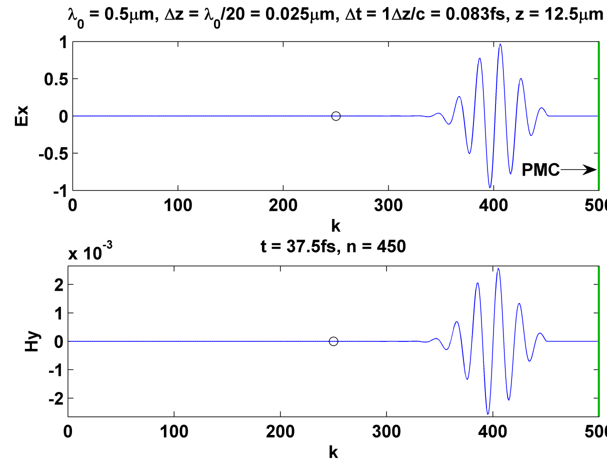

(a) Pulse approaching the PMC at t=37.5fs and n=450.

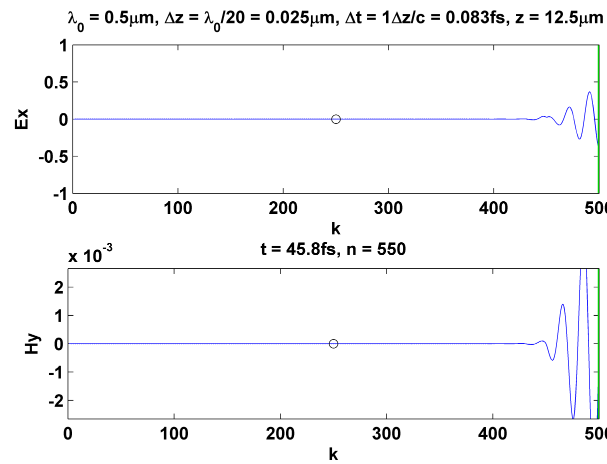

(b) Pulse colliding with the PMC at t=45.8fs and n=550.

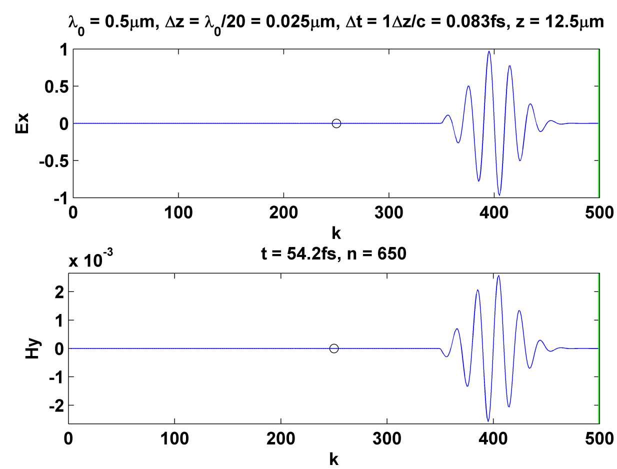

(c) Pulse reflected from the PMC at t=54.2fs and n=650.

Fig. 10. $E_x(k)$ and $H_y(k)$ (a) before the PMC at t=37.5fs (b) colliding with the PMC at t=45.8fs and (c) reflected from the PMC at t=54.2fs. Notice the constructive interference between the incident H_y and the reflected H_y at (b); because H_y and E_x differ in phase after reflection, while H_y is constructive interfering with its tail, E_x is destructive interfering with his. This is why E_x shows less than unity amplitude compared to H_y in (b).

Fig. 9 displays E_x and H_y fields at the probe location of $k = 250$ and $k = 250.5$ respectively, for a total simulation duration of 83.3fs; it clearly shows that the PMC at $z = z_{max}$ or $n = 500$ caused H_y to invert while leaving E_x un-altered.

D. Grid dispersion

The previous PEC and PMC results were obtained at the magic time step where $\Delta t = \Delta z/c$. In this section, we will examine what happens to the pulse shape on both passes through the probe for the PEC case when $\Delta t \neq \Delta z/c$ but $\leq \Delta z/c$.

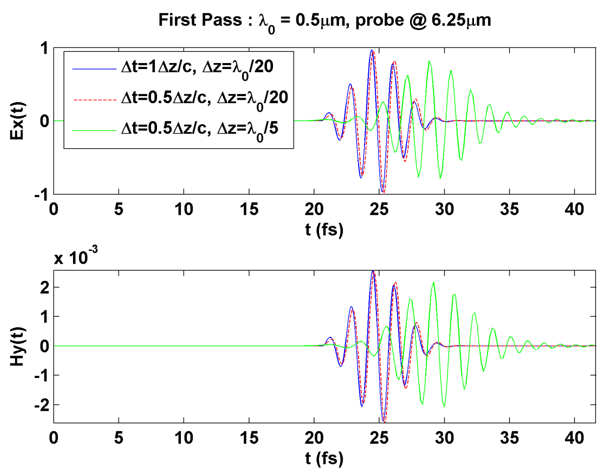

(a) First pass through the probe.

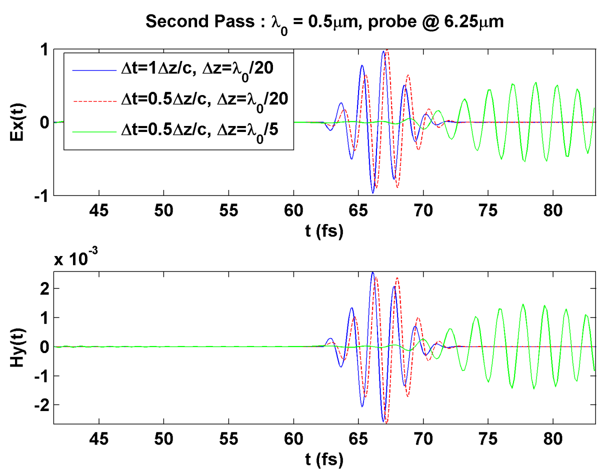

(b) Second pass after reflection from PEC.

Fig. 11. Comparison of probe data $E_x(t)$ and $H_y(t)$ during the first pass (a) and the second pass (b) after reflecting from the PEC for ($\Delta t = \Delta z/c$, $\Delta z = \lambda_0/20$), ($\Delta t = 0.5\Delta z/c$, $\Delta z = \lambda_0/20$), and ($\Delta t = 0.5\Delta z/c$, $\Delta z = \lambda_0/5$).

Using the numerical dispersion diagram of Fig. 12, duplicated from [3] as a guide: first, we let $\Delta t = 0.5\Delta z/c$ but keep $\Delta z = \lambda_0/20$ the same to see the shift of the pulse phase with respect to the pulse envelope; this corresponds to the red operating point of Fig. 12; second, in addition to operating at $\Delta t = 0.5\Delta z/c$ we adjust the spatial sampling from $\Delta z = \lambda_0/20$ to $\Delta z = \lambda_0/5$ and observe changes in the pulse velocity (this corresponds to the green operating point of Fig. 12). We are essentially performing simulations at different points on the red ($c\Delta t = \Delta x/2$) curve, keeping in mind that Δx is our Δz.

From Fig. 11, we see that for the case $\Delta z = \lambda_0/20$, comparison between the ideal pulse propagating at the magic time step (blue) to the case where $\Delta t = 0.5\Delta z/c$ (red) shows

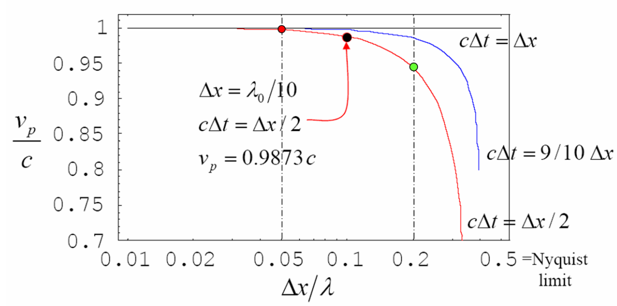

Fig. 12. Phase velocity relative to c as a function of space and time griding [3]. The red and green dots corresponds to the operating point of red and green curves in Fig. 11.

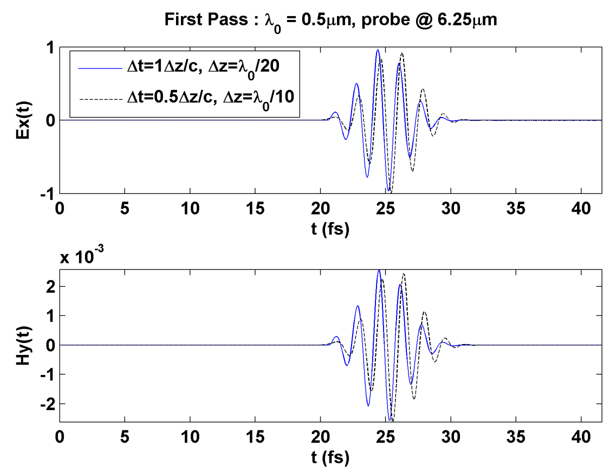

(a) First pass through the probe.

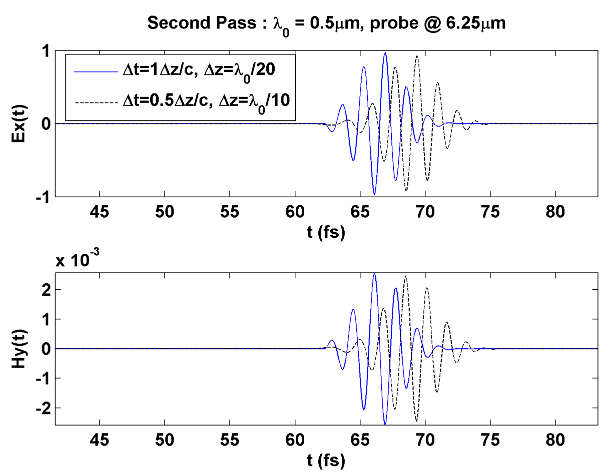

(b) Second pass after reflection from PEC.

Fig. 13. Comparison of probe data $E_x(t)$ and $H_y(t)$ during the first pass (a) and the second pass (b) after reflecting from the PEC for ($\Delta t = \Delta z/c$, $\Delta z = \lambda_0/20$), and ($\Delta t = 0.5\Delta z/c$, $\Delta z = \lambda_0/10$).

that grid dispersion increases with increasing propagation distance and induces phase shift and distortion to the pulse. During the first pass Fig. 11(a), the off-magic-time pulse (red) shows slight phase delay when compared to the magic-time pulse (blue); however by the second pass after the pulse reflected from the PEC in Fig. 11(b), not only was the pulse phase delayed further when compared to the original envelope but its shape was distorted; what appears to be an odd pulse before, now appears even. The result is even more dramatic in (green) of Fig. 11, where the increase in Δz by a factor of 4 to $\lambda_0/5$ not only widened the pulse but also reduced its phase velocity, i.e., the green pulse arrived late at the probe compared to both the blue and red pulses. This is to be expected from the dispersion diagram of Fig. 12, where the phase velocity degradation due to grid dispersion at the green operating point is predicted to be about 5%. To save computational resources, it is common practice to use $\Delta z = \lambda_0/10$ and $\Delta t = 0.5\Delta z/c$ to limit the amount dispersion (phase error); this case is shown in Fig. 13.

E. First-order Mur radiation boundary

In this section, we will enforce a first-order Mur radiation/absorbing boundary condition (ABC) at $z = z_{max} = 12.5\mu m$ and test its operation first at the magic time step.

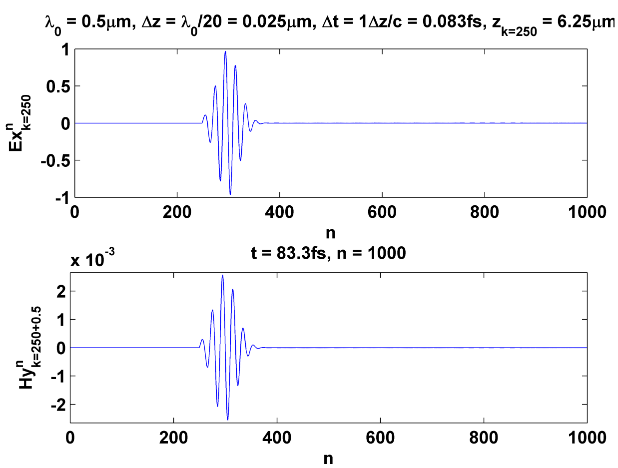

Fig. 14. Mur probe data of E_x and H_y at grid position $k = 250$ and $k = 250.5$ as a function of time step n. $\Delta z = \lambda_0/20$ and $\Delta t = \Delta z/c$. The total simulated duration was 83.3fs or $n = 1000$.

Letting the simulation run for the same duration $t = 83.3$fs as was previously done for the PEC and PMC cases, we find from the probe data of Fig. 14 that the pulse only pass the probe once, indicating that it has indeed radiated or absorbed by the Mur at $z = z_{max}$. Fig. 15 shows snap shots of the Mur boundary in action. Although the Mur boundary worked perfectly for the magic time step, due to the use of centered differences and the order of approximation, this boundary will be imperfect when operating off the magic time step. An estimate of the reflectivity of the first-order Mur boundary at $\Delta z = \lambda_0/10$ and $\Delta t = 0.5\Delta z/c$ can be found using the following equation [3]:

$$|r_{mur1}| = \frac{a-b}{a+b} \approx 0.0131; \tag{25}$$

where

$$a = \Delta z \sin(\omega_0 \Delta t/2)\cos(k_z \Delta z/2), \tag{26}$$
$$b = c\Delta t \cos(\omega_0 \Delta t/2)\sin(k_z \Delta z/2). \tag{27}$$

Simulation validation of the 0.0131 reflectance from equation (25) can be estimated from peak field values of the incident and reflected pulse using the time domain probe data of Fig. 16 or more accurately determined by the ratio of their Fourier transforms, see Fig. 17.

The maximum peak value of the incident electric field from

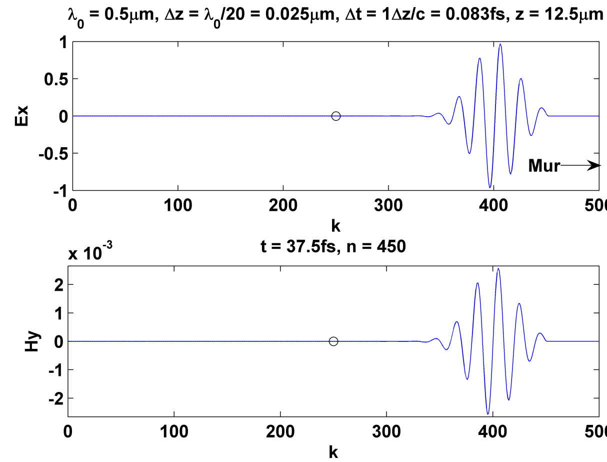

(a) Pulse approaching the ABC at t=37.5fs and n=450.

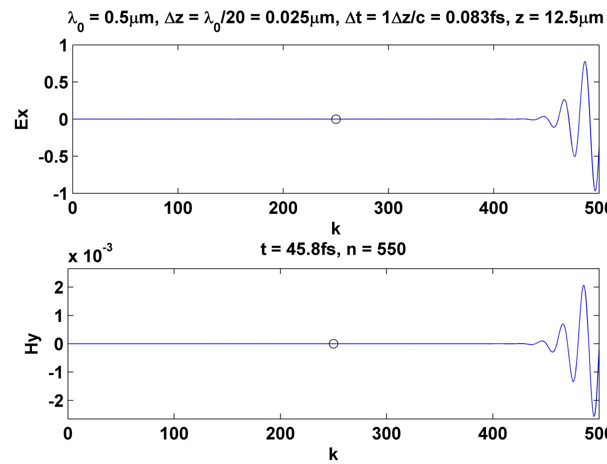

(b) Pulse entering the ABC at t=45.8fs and n=550.

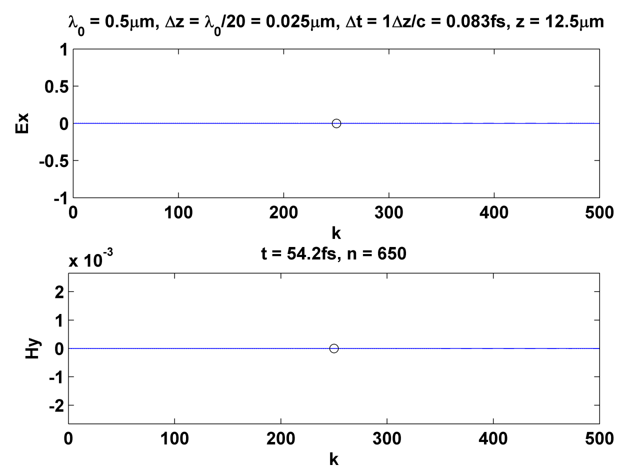

(c) Pulse absorbed by the ABC at t=54.2fs and n=650.

Fig. 15. $E_x(k)$ and $H_y(k)$ (a) before the ABC at t=37.5fs (b) entering the ABC at t=45.8fs and (c) absorbed by the ABC at t=54.2fs. $\Delta z = \lambda_0/20$ and $\Delta t = \Delta z/c$.

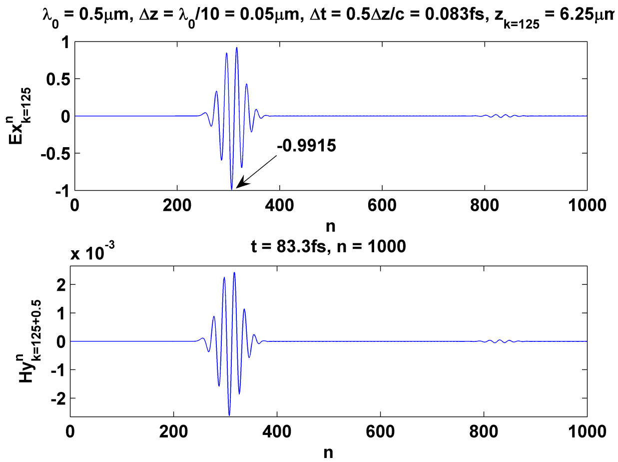

(a) Total probe data.

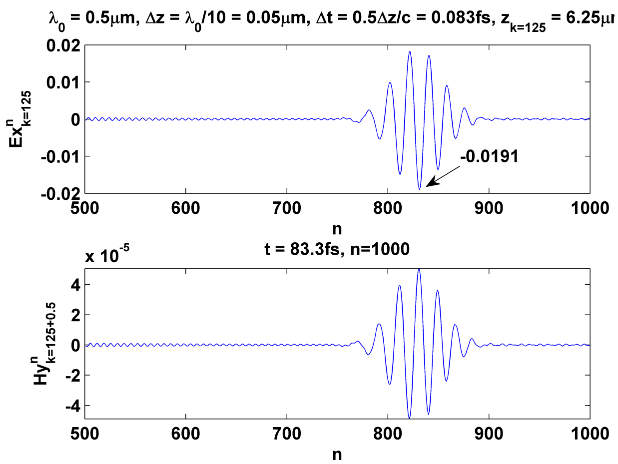

(b) Scattered half of the probe data with better scaling.

Fig. 16. Mur probe data (a) of E_x and H_y at grid position $k = 125$ and $k = 125.5$ as a function of time step n. (b) is the second half of (a) (scattered only) shown with better scaling. $\Delta z = \lambda_0/10$ and $\Delta t = 0.5\Delta z/c$. The total simulated duration was 83.3fs or $n = 1000$.

Fig. 16 is -0.9915(V/m) and the maximum peak value of the reflected electric field is -0.0191(V/m); their ratio is ≈ 0.0193 which is higher than (25)'s estimate of 0.0131. Repeating the exercise using the magnitude of the Fourier transforms of the incident and reflected pulse Fig. 17 produced a reflectance of 0.0199 at f_0 of 0.6PHz.

F. Scattered/Total Boundary

At a distance of approximately 1/3 of the way into the mesh from $z = 0$, we added a scattered/total field boundary. Fig. 18 demonstrates that both $E_x(k)$ and $H_y(k)$ only propagate towards the positive z direction. Notice the reason it took the pulse about 16.7fs to emerge from the SF/TF boundary has to do with the fact that we have propagated an E_{inc} and H_{inc} on its own 1D-FDTD grid starting at node $z = 0$ and they need to first travel 1/3 of the total z to reach the SF/TF boundary.

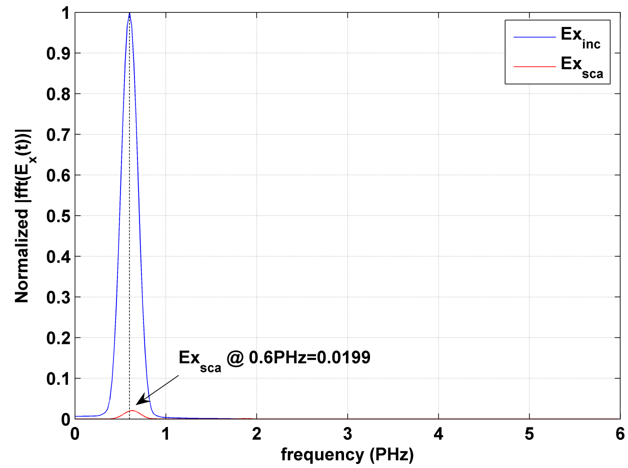

Fig. 17. Discrete Fourier transform of the incident and reflected $E_x(t)$ in the case of Mur boundary operating at $\Delta z = \lambda_0/10$ and $\Delta t = 0.5\Delta z/c$.

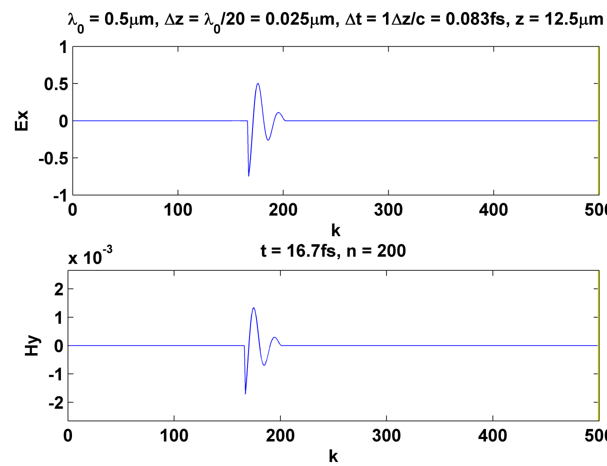

(a) Pulse emerging from SF/TF boundary at t=16.7fs and n=200.

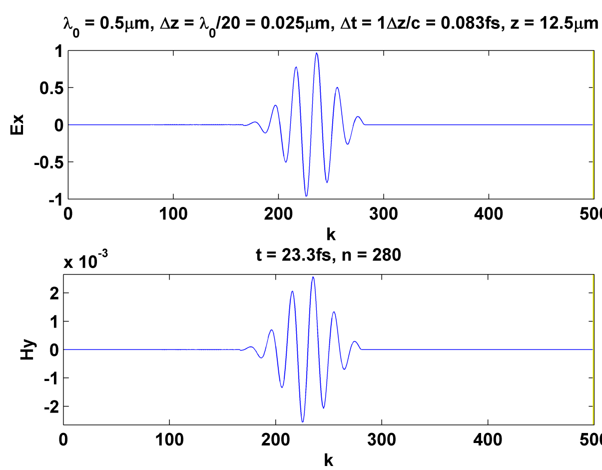

(b) Pulse entered space grid at t=23.3fs and n=280.

Fig. 18. $E_x(k)$ and $H_y(k)$ (a) emerging from the SF/TF boundary (b) entered completely into the space grid. This is essentially an unidirectional pulse.

IV. Dielectric Slab

In this section, we implement the same first-order Mur condition on boundaries $z = 0, z = z_{max} = 12.5\mu m$; additionally we add a dielectric array (slab) of refractive index $n = 1.5$ on the same sampling grid as the electric field array at about 2/3 of the way and filled the rest with air $n = 1$.

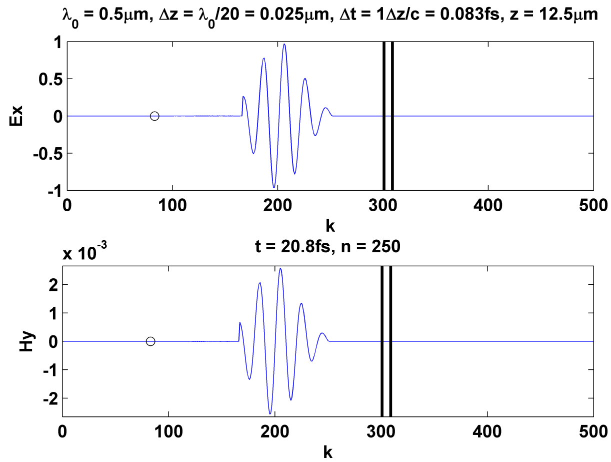

(a) Pulse emerging from SF/TF boundary.

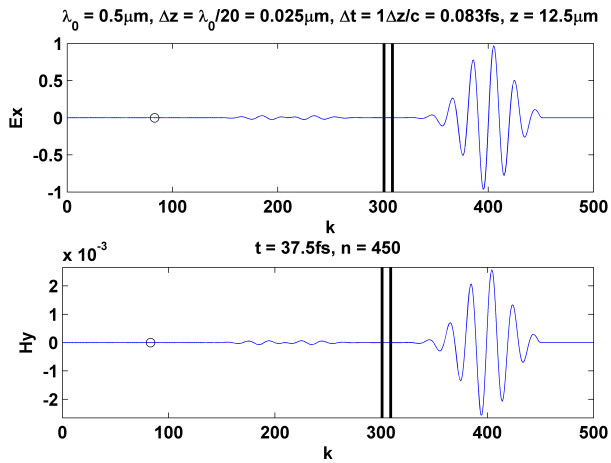

(b) Pulse reflected and transmitted after hitting the dielectric slab.

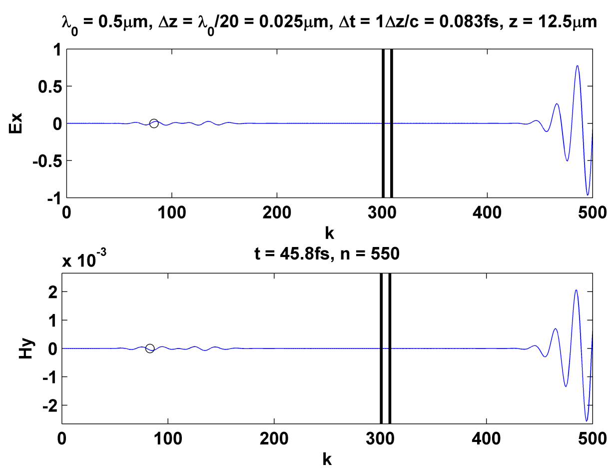

(c) Transmitted pulse gets absorbed by the Mur while the reflected pulse approaches the probe.

Fig. 19. $E_x(k)$ and $H_y(k)$ at various instances in time impinging on a dielectric slab of index $n = 1.5$, thickness $\lambda_g/2 = 0.204\mu m$

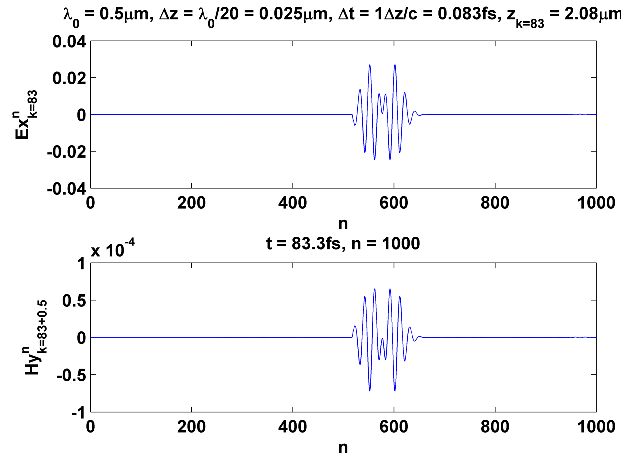

(a) Scattered field probe data of E_x and H_y for the $\lambda_g/2$ thick slab case shown in Fig. 19.

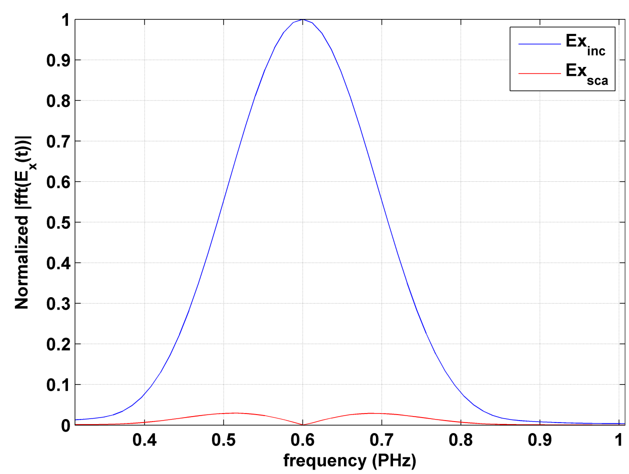

(b) Discrete Fourier transform of the incident and scattered $E_x(t)$ in (a).

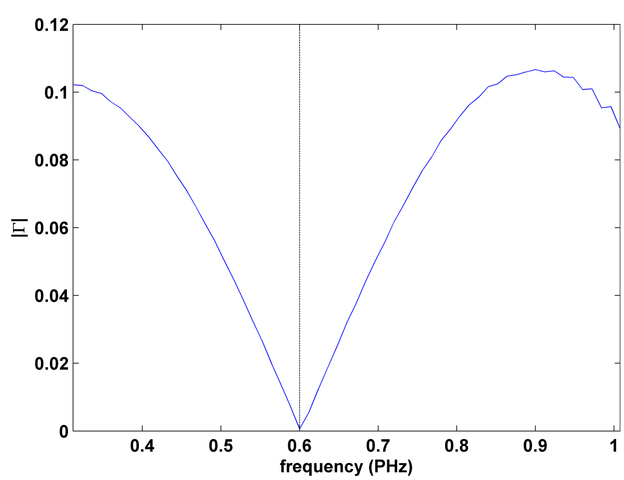

(c) Magnitude of the reflection coefficient obtained by the ratio of the scattered to incident Fourier transforms of (b).

Fig. 20. (a)Scattered field probe data of E_x and H_y of the $\lambda_g/2 = 0.204\mu m$ thick slab. (b) Discrete Fourier transform of the incident and scattered $E_x(t)$ in (a). (c) Magnitude of the reflection coefficient from $f = 0.3$ to $f = 1$PHz corresponding to $\lambda_0 = 1\mu m$ to $\lambda_0 = 300nm$.

For accuracy, we choose to operate at the magic time step $dt = dz/c$ with $dz = \lambda_0/20$. The scattered electric field is measured by a probe placed in the scattered field region about 1/6 of the the total distance at $z = 2.08\mu m$.

Figures (20-21) show the initial simulation using standard

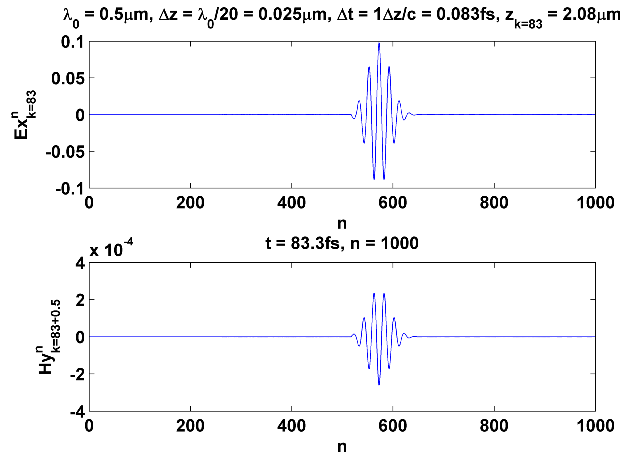

(a) Scattered field probe data of E_x and H_y for the $\lambda_g/4$ thick slab case.

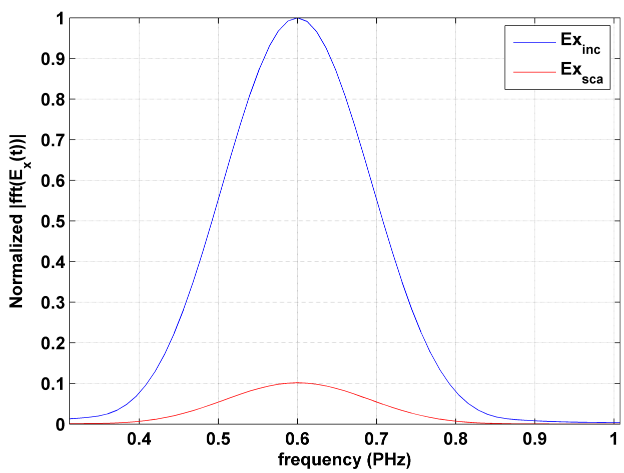

(b) Discrete Fourier transform of the incident and scattered $E_x(t)$ in (a).

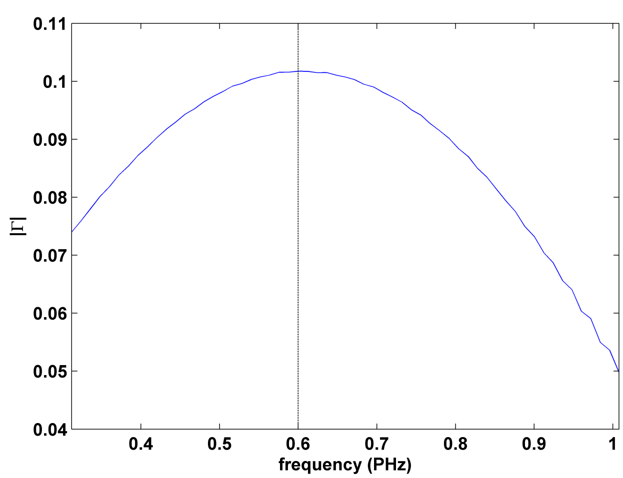

(c) Magnitude of the reflection coefficient obtained by the ratio of the scattered to incident Fourier transforms of (b).

Fig. 21. (a)Scattered field probe data of E_x and H_y of the $\lambda_g/4 = 0.102\mu m$ thick slab. (b) Discrete Fourier transform of the incident and scattered $E_x(t)$ in (a). (c) Magnitude of the reflection coefficient from $f = 0.3$ to $f = 1$PHz corresponding to $\lambda_0 = 1\mu m$ to $\lambda_0 = 300nm$.

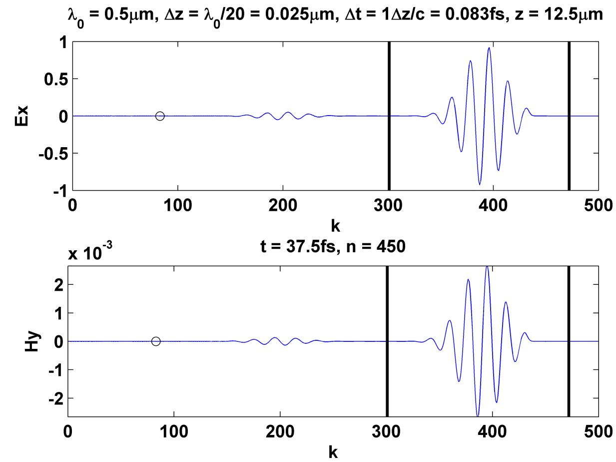

(a) Pulse reflected from the front face of the slab.

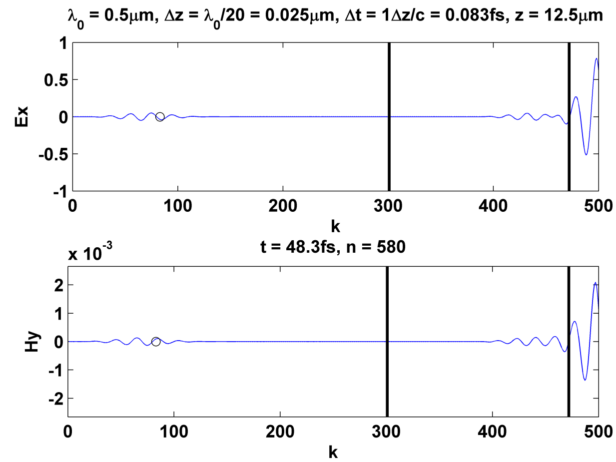

(b) Pulse reflected from the back face of the slab.

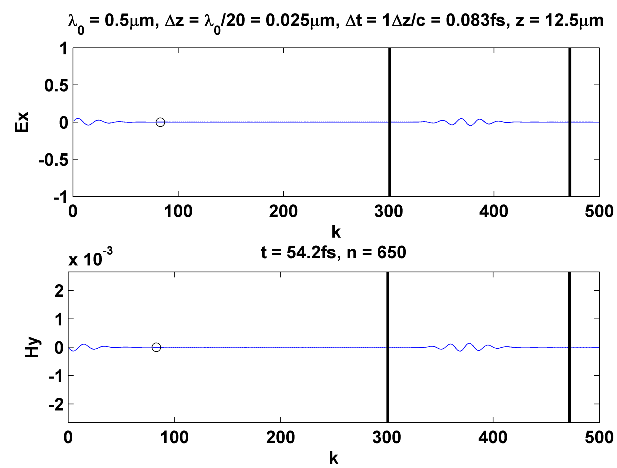

(c) Pulse absorbed by the Mur ABC on the left of the space grid.

Fig. 22. $E_x(k)$ and $H_y(k)$ at various instances in time impinging on a dielectric slab of index $n = 1.5$, thickness $10.5\lambda_g = 4.284\mu m$

$\lambda_g/2$ and $\lambda_g/4$ thick dielectric slabs; they clearly indicate that at these slab thicknesses, the incident pulse experiences minimum and maximum reflection, respectively.

Because sub-wavelength optical components are difficult to manufacture, it is common to add a multiple λ_g to the basic $\lambda_g/4$ or $\lambda_g/2$ plate thicknesses; however, from Figures (23-24) we find that increasing the plate thickness reduces the

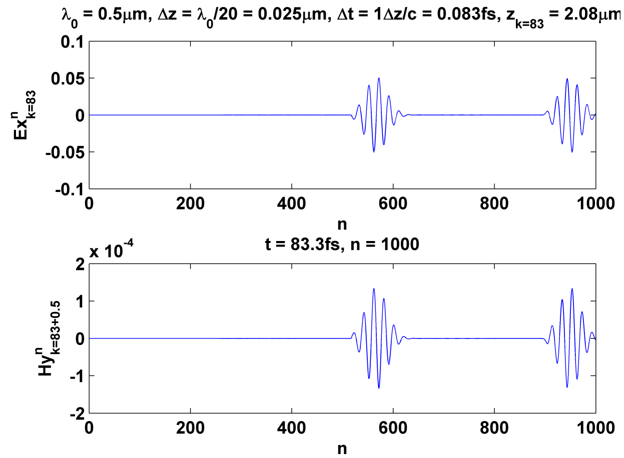

(a) Scattered field probe data of E_x and H_y for the $10.5\lambda_g = 4.284\mu m$ thick slab case shown in Fig. 22.

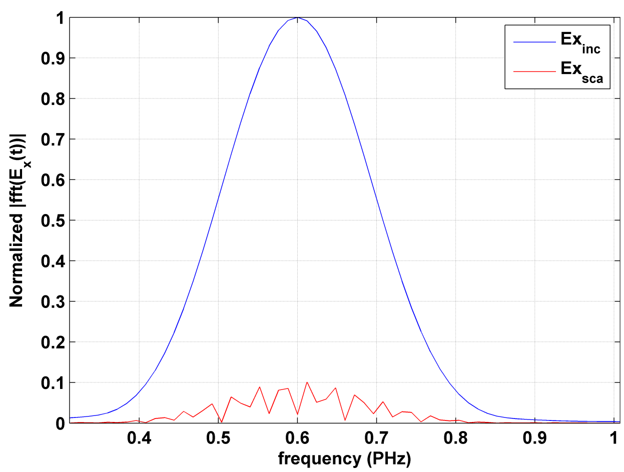

(b) Discrete Fourier transform of the incident and scattered $E_x(t)$ in (a).

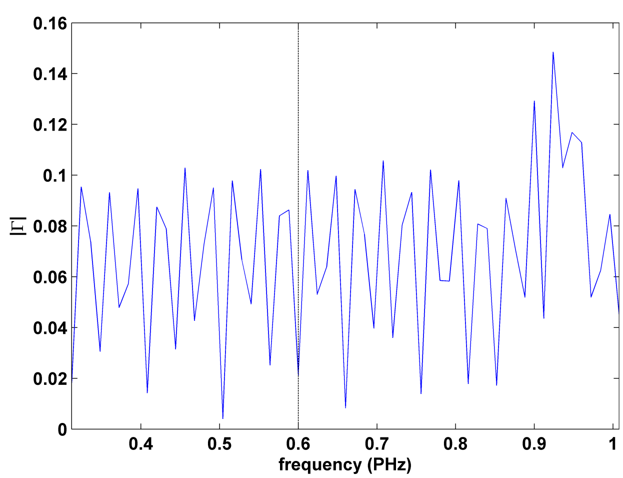

(c) Magnitude of the reflection coefficient obtained by the ratio of the scattered to incident Fourier transforms of (b).

Fig. 23. (a) Scattered field probe data of E_x and H_y of the $10.5\lambda_g = 4.284\mu m$ thick slab. (b) Discrete Fourier transform of the incident and scattered $E_x(t)$ in (a). (c) Magnitude of the reflection coefficient from $f = 0.3$ to $f = 1$PHz corresponding to $\lambda_0 = 1\mu m$ to $\lambda_0 = 300nm$.

low-reflectivity bandwidth drastically.

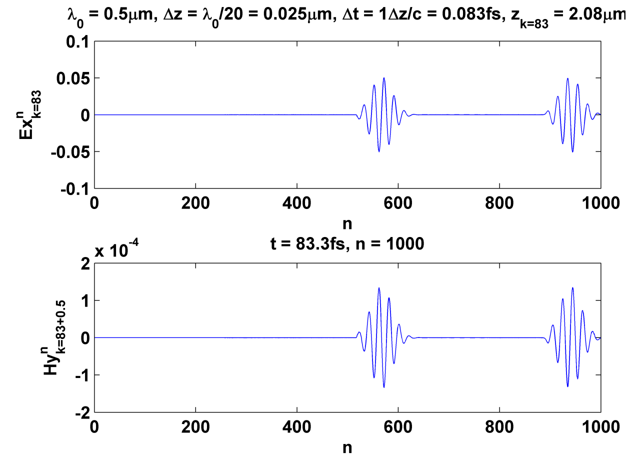

(a) Scattered field probe data of E_x and H_y for the $10.25\lambda_g = 4.182\mu m$ thick slab case.

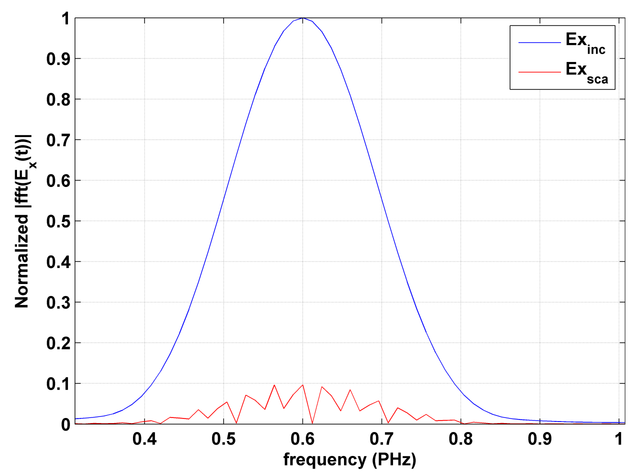

(b) Discrete Fourier transform of the incident and scattered $E_x(t)$ in (a).

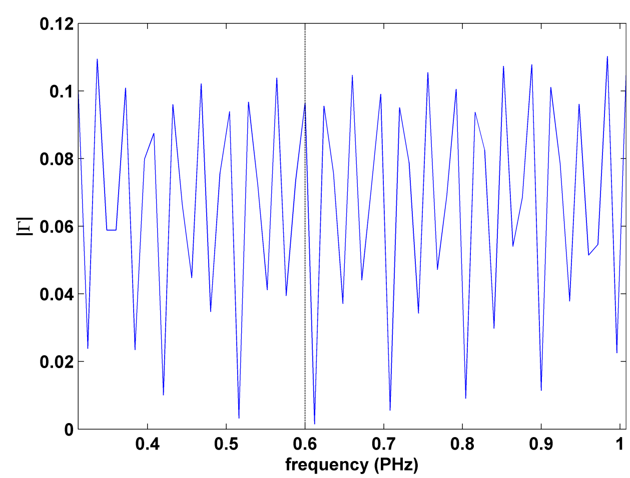

(c) Magnitude of the reflection coefficient obtained by the ratio of the scattered to incident Fourier transforms of (b).

Fig. 24. (a) Scattered field probe data of E_x and H_y of the $10.25\lambda_g = 4.182\mu m$ thick slab. (b) Discrete Fourier transform of the incident and scattered $E_x(t)$ in (a). (c) Magnitude of the reflection coefficient from $f = 0.3$ to $f = 1$PHz corresponding to $\lambda_0 = 1\mu m$ to $\lambda_0 = 300nm$.

V. Conclusion

This paper successfully demonstrates a working 1D-FDTD code that correctly implements PEC, PMC, Mur and SS/TF boundaries. The code is applied to investigate pulse reflections from dielectric slabs of various thickness; it is found through simulation that $\lambda_g/2$ and $\lambda_g/4$ thick dielectric slabs produce the minimum and maximum reflection, respectively. Increasing the thickness of the slabs drastically reduces the low-reflectivity bandwidth. We have also shown that grid dispersion occurs when one operates off the magic-time-step; it delays the pulse phase and distorts the pulse shape.

ACKNOWLEDGMENT

I would like to thank professor Robert McLeod for his active interaction with me during the coding process. I learned a lot.

REFERENCES

[1] A. Taflove and S. Hagness, *Computational Electrodynamics - the finite difference time-domain method*, 2nd ed. Norwood, MA: Artech House, 2000, pp. 197–201.

[2] D. M. Sullivan, *Electromagnetic Simulation using the FDTD Method*. Piscataway, NY: IEEE Press, 2000.

[3] R. R. McLeod, “Finite difference time domain class notes,” pp. 31–59, Sept. 2004.

[4] K. S. Yee, “Numerical solution of initial boundary value problems involving maxwell’s equations in isotropic media,” *IEEE Trans. Antennas Propagat.*, vol. 14, pp. 302–307, 1966.

[5] E. W. Weisstein, “Gaussian function,” *MathWorld–A Wolfram Web Resource, http://mathworld.wolfram.com/GaussianFunction.html*, 2004.

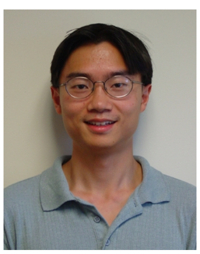

Hung Loui (S’02) received BSEE and BM (piano performance) degrees from the University of Colorado at Boulder, in 2001, and is currently pursuing a Ph.D in Electromagnetics. From 1997 to 2001, he did his undergraduate research at the Laboratory for Atmospheric and Space Physics (LASP) where he was responsible for the design, production and characterization of the instrumental scientific data processing (DSP) boards aboard the Solar Radiation and Climate Experiment (SORCE) satellite. While at LASP, he was also involved in the design and integration of the (CHAMP) microscope camera with the prototype K9 Mar’s rover and participated in the dust particle collisions in planetary rings (COLLIDE) project. In music, he has performed classical piano concertos with both the Grand Junction Symphony, Grand Junction, CO and the university orchestra.